Chemical Engineering Journal 513 (2025) 163083

Contents lists available at ScienceDirect

Chemical Engineering Journal

journal homepage: www.elsevier.com/locate/cej

Improved water stability by thermal treatment of hexatopic ligand-based metal-organic frameworks for hydrogen storage

Hong-Eun An [a,b,1], Wan-Tae Kim [a,1], Dong Yun Shin [c], SeJin Park [d], Eunki Yoon [e], Dae Won Kim [f], Chang Seop Hong [f], Soohyung Park [e], Hyunchul Oh [d], Jung-Hoon Lee [c,g,*], Sohee Jeong [a,*]

[a] Materials Architecturing Research Center, Korea Institute of Science and Technology (KIST), Seoul 02792, Republic of Korea
[b] Department of Materials Science and Engineering, Korea University, Seoul 02841, Republic of Korea
[c] Computational Science Research Center, Korea Institute of Science and Technology (KIST), Seoul 02792, Republic of Korea
[d] Ulsan National Institute of Science and Technology (UNIST), Ulsan 44919, Republic of Korea
[e] Advanced Analysis and Data Center, Korea Institute of Science and Technology (KIST), Seoul 02792, Republic of Korea
[f] Department of Chemistry, Korea University, Seoul 02841, Republic of Korea
[g] KU-KIST Graduate School of Converging Science and Technology, Korea University, Seoul 02841, Republic of Korea

ARTICLE INFO

Keywords:
Metal–organic frameworks
Water stability
Thermal treatment
Hexatopic ligand
Hydrogen storage

ABSTRACT

One of the essential properties required for the practical application of metal–organic frameworks (MOFs) as gas storage materials is high water stability. In this study, we investigate the origin of improved water stability through thermal treatment in V_3(PET), a MOF containing hexatopic peripherally extended triptycene (H_6PET) ligands, which show promise for hydrogen storage. While V_3(PET) should be water-stable due to strong metal (hard acid, V^{3+})-ligand (hard base, carboxylate group) bonds, our experimental and theoretical findings reveal that the presence of dangling ligand—defects caused by metal-modulator (acetate) bonds— reduces its water stability. Our first-principles density functional theory (DFT) calculations show that the defect formation energy for V_3(PET) with dangling ligands (+1.96 eV) is significantly lower than that for V_3(PET) without them (+6.34 eV), making it more vulnerable to humidity. By removing acetate and restoring the original metal–ligand bonds, we significantly enhance the water stability of V_3(PET). Additionally, thermally treated V_3(PET) retains about 95 % of its hydrogen storage performance even after 7 days in 60 % relative humidity and maintains high mechanical stability over 200 hydrogen storage cycles.

1. Introduction

Hydrogen is a promising energy carrier due to its highest energy density per unit mass (120 MJ/kg) and status as a clean energy source, with water being the only combustion product when used in fuel cells or combustion [1,2]. However, storing it as compressed gas at up to 700 bar requires substantial energy and presents safety risks [3,4]. Metal-organic frameworks (MOFs) are one of the promising material classes for hydrogen storage owing to their high surface areas and fast adsorption/desorption kinetics under relatively mild conditions [5–10]. However, challenges such as the difficulty of large-scale synthesis, a low hydrogen storage capacity at room temperature, and poor water stability still remain [11,12]. Among these, the structural instability of MOFs in the presence of water is mainly responsible for the degradation of the gas storage performance under humid conditions [13,14]. This is particularly problematic for industrial processes involving materials preparation and storage, where gaseous or liquid water is inevitably present [15–17].

Thus, different experimental and theoretical studies have tried to improve the water stability of MOFs. For instance, protection strategies against water access, such as hydrophobic polymer coating on the surface of MOFs and substitution of hydrophobic ligands, have been widely adopted due to their effectiveness [18–20]. However, modifying MOFs by exchanging hydrophobic ligands or hydrophobic polymer coating could lead to a loss of porosity and an increase in inactive mass, which reduces the overall performance in hydrogen storage applications [21–23]. Additionally, their application to MOFs with complex ligand architectures (high denticity) is often hindered by slow kinetics during

---

[*] Corresponding authors at: Korea Institute of Science and Technology (KIST), Materials Structure Research Center, Seoul 02792, Republic of Korea.
E-mail addresses: jhlee84@kist.re.kr (J.-H. Lee), soheejeong@kist.re.kr (S. Jeong).

[1] Hong-Eun An and Wan-Tae Kim contributed equally to this work.

https://doi.org/10.1016/j.cej.2025.163083
Received 3 December 2024; Received in revised form 21 March 2025; Accepted 24 April 2025

the exchange process [24]. Moreover, these approaches typically require additional processing steps, such as solvent-based stirring, re-drying, and re-activation, which complicate large-scale implementation. In contrast, thermal treatment provides a simple and scalable approach to enhance water stability without requiring additional chemical modifications or post-synthetic processing steps [25,26].

On the other hand, theoretical studies have also aimed to design MOFs with inherent high water stability [27,28]. The hard soft acid base (HSAB) theory has been widely used as a representative theoretical standard for designing highly stable MOFs. According to the HSAB theory, MOFs with hard acid metals (Zr^{4+}, Al^{3+}, Fe^{3+}, V^{3+}, Ti^{4+})–hard base ligands (carboxylate-based ligands) or soft acid metals (Zn^{2+}, Co^{2+}, Ni^{2+}, Cu^{2+})–soft base ligands (azolate-based ligands) combinations exhibit relatively high water stability [14,29]. However, in some MOFs structures designed by the HSAB theory, the presence of defects within the MOFs can result in lower water stability [30,31].

According to previous studies [32–34], different defects can be easily formed even in different MOF structures. For example, modulators used to improve the crystallinity of MOFs inevitably remain at ligand sites and cause defects, which are called missing ligand defects or dangling ligands [35–38]. When a modulator remains in the MOFs composed of ditopic ligands (*e.g.,* terephthalic acid), a missing ligand defect is generally induced [39–42]. In this case, additional open metal sites and large pore space could be created by removing modulators within the pore through thermal treatment [42,43]. This can have a detrimental impact on the water stability of MOFs as water molecules penetrate into MOF’s structures and then disrupt the metal–ligand coordination bonds at the metal nodes [44–46].

Despite various experimental studies investigating the effects of ligand defects on the structural properties and related water stability of MOFs, a detailed understanding of the role of ligand defects in the water stability of MOFs is still lacking. In particular, the atomic-scale mechanisms are not well understood. Here, we investigate the water stability of our recently developed MOF, V_3(PET) [47], which exhibits a total hydrogen uptake of 8.4 wt% and 46.7 g/L at 77 K and 100 bar, comparable to high-performance MOFs such as MOF-5 and SNU-70. Given its promising hydrogen storage capacity, understanding its stability under humid conditions is essential for assessing its practical applicability. We further clarify the mechanism behind its improved water stability, achieved through a simple and effective thermal treatment process. We found that thermally treated V_3(PET) maintained 92 % porosity under 60 % relative humidity (RH) at 25 °C for 72 h, whereas bare V_3(PET) completely lost its porosity. Our experiments and DFT calculations revealed a mechanism distinct from the conventional understanding, which suggests that amorphous carbon coatings formed by thermal treatment block water molecules from penetrating the structure [25,26]. Specifically, we found that residual acetate units (modulators) bound to V^{3+} metals are mainly responsible for the poor water stability of bare V_3(PET) despite the presence of strong hard acid metal (V^{3+})–hard base ligand bonds as described by the HSAB theory. In contrast, thermal treatment effectively removed acetate units in V_3(PET), thereby restoring the original metal–ligand bonds of the destabilizing dangling ligands, which significantly enhanced the structure stability. This stabilization is facilitated by the hexatopic nature of PET ligands, indicating that ligand denticity plays a crucial role in the thermal treatment mechanism of enhanced water stability of V_3(PET). Our DFT calculations further showed that the ligand defect formation energy in defect-free bare V_3(PET) is much more stable than that in V_3(PET) with acetate-induced dangling ligands, showing higher resistance to water exposure. Additionally, we observed that thermally treated V_3(PET) maintained its good performance for hydrogen adsorption, even in the presence of water.

2. Experimental section

2.1. Materials and analytical equipment

All chemicals were used without further purification. The compounds VCl_3(tetrahydrofuran)$_3$ ($VCl_3(THF)_3$), acetonitrile, acetic acid, Vanadium (III) chloride (VCl_3) and terephthalic acid (H_2BDC) were purchased from Sigma Aldrich Co., Ltd, while 4,4′,4′’,4′’’,4′’’’,4′’’’’-(9,10-dihydro-9,10-[1, 2,]benzenoanthracene-2,3,6,7,14,15-hexayl) hexabenzoic acid (hexatopic peripherally extended triptycene, H_6PET) was purchased from Chemsoon Co., Ltd, N,N-dimethylformamide (DMF) and acetone were purchased from Daejung Co., Ltd. In addition, trimesic acid (H_3BTC) was purchased from Alibaba, tetrakis(4-carboxyphenyl) porphyrin (H_6TCPP) was purchased from Tokyo Chemical Industry Co., Ltd., Copper(II) nitrate trihydrate ($Cu(NO_3)_2{\cdot}3H_2O$) was purchased from Thermo Fisher Scientific co. Ltd.

Scanning electron microscope (SEM, Inspect F, FEI Company), X-ray diffractometer (D8 Advance, Bruker AXS Inc.), X-ray photoelectron spectrometer (XPS, Nexsa, Thermo Fisher Scientific Inc.), thermogravimetric analyzer (TGA), Fourier transform infrared spectrometer (FT-IR, Perkin Elmer Frontier, PerkinElmer Inc.), Raman spectrometer (inVia Reflex, Renishaw with the laser excitation wavelength of 532 nm), nuclear magnetic resonance (NMR, Avance III HD 400 MHz), gas adsorption analyzer (ASAP 2020), Liquid Chromatography-Mass Spectrometry system (LC-MS, SYNAPT G2-S) and Electron paramagnetic resonance (EPR, Bruker EMXplus-9.5/2.7) spectrometer were used for materials characterization. Near-edge X-ray absorption fine structure (NEXAFS) spectroscopy was conducted at the 10D KIST-PAL beamline in the Pohang Accelerator Laboratory (PAL).

2.2. Synthesis of V_3(PET)

$VCl_3(THF)_3$ (139 mg, 0.373 mmol) and H_6PET (30 mg, 0.031 mmol) were mixed in 5 mL of DMF, 5 mL of acetonitrile, and 0.5 mL acetic acid in a 50 mL glass bottle, and then the mixture was sonicated for 30 min. The mixture was heated to 150 °C for 48 h. The precipitated MOFs were centrifuged to separate them from the mother liquor. The product was washed 3 times with 30 mL of DMF and immersed in 30 mL of DMF overnight. It was centrifuged again, washed 6 times with 30 mL of acetone, and immersed in 30 mL of acetone for 2 days. The acetone was decanted, and the samples were activated under vacuum at 120 °C for 12 h to yield 28 mg (76 %) of $V_3O(OH)$(PET) (V_3(PET)) as a green microcrystalline solid.

2.3. Synthesis of MIL-101

MIL-101 was synthesized using the synthesis method of Biswas, Shyam, et al. [48]. VCl_3 (200 mg, 1.27 mmol) and H_2BDC (106 mg, 0.64 mmol) were mixed in 2 mL of DMF and 0.1 mL of acetic acid in a 10 mL glass bottle, and then the mixture was sonicated for 30 min. The mixture was heated to 150 °C for 24 h. The precipitated MOFs were centrifuged to separate them from the mother liquor. The product was washed 3 times with 30 mL of DMF and washed 3 times with 30 mL of acetone. The acetone was decanted, and the samples were activated under vacuum at 130 °C for 12 h.

2.4. Synthesis of HKUST-1

HKUST-1 was synthesized using a previously reported method with minor modifications [49,50]. $Cu(NO_3)_2{\cdot}3H_2O$ (1,038 mg, 4.03 mmol) was dissolved in 30 ml water. H_3BTC (500 mg, 2.38 mmol) was dissolved in 30 mL of ethanol, 30 ml of DMF, and 1.25 mL of acetic acid. The two solutions were mixed directly in a 100 mL Teflon-lined autoclave. The mixture was sonicated for 30 min and then heated to 100 °C for 18 h. The precipitated MOFs were centrifuged to separate them from the mother liquor. The product was washed several times with DMF and methanol. The methanol was decanted, and the samples were activated under vacuum at 120 °C for 12 h.

2.5. Synthesis of Cu-TCPP

Cu-TCPP was synthesized using a previously reported method with minor modifications [51]. $Cu(NO_3)_2 \cdot 3H_2O$ (500 mg, 2.07 mmol) and H_6TCPP (100 mg, 0.13 mmol) were mixed in 80 mL of DMF and 1.2 mL of acetic acid in a 100 mL glass bottle. The mixture was sonicated for 30 min and then heated to 80 °C for 24 h. The product was washed 3 times with 30 mL of DMF and washed 3 times with 30 mL of ethanol. The ethanol was decanted, and the samples were activated under vacuum at 120 °C for 12 h.

2.6. Synthesis of Ga_3(PET)

Ga_3(PET) was synthesized using a previously reported method with minor modifications [47]. $Ga(NO_3)_3 \cdot xH_2O$ (475 mg) and H_6PET (150 mg, 0.15 mmol) were mixed in 25 mL of DMF, 25 mL of acetonitrile, and 15 mL of acetic acid in a 250 mL glass bottle. The mixture was sonicated for 30 min and then heated to 150 °C for 48 h. The product was washed 3 times with 30 mL of DMF and washed 3 times with 30 mL of acetone. The acetone was decanted, and the samples were activated under vacuum at 120 °C for 12 h.

2.7. Thermal treatment

All samples were stored in a glove box before thermal treatment to minimize exposure to ambient air and moisture. All samples were heated in an external tube with a 150 mL/min Ar flow while in the activated state. The furnace heated at a rate of 5 °C/min, maintained each sample at a specific thermal treatment temperature—determined based on TGA analysis—for 30 min, and then cooled them to room temperature. Each thermal-treated sample was named '(sample name)@(thermal treatment temperature)' (e.g., V_3(PET)@400).

2.8. Water stability test

All samples underwent the activation process and were then exposed to 60 % relative humidity (RH) at 25 °C in a temperature and humidity chamber (S-TH31).

2.9. Solution-state ^1H NMR measurements

All samples were activated and digested with DCl (16 μL, 35 wt% in D_2O) in DMSO-d_6 (1 mL) under sonication for 30 min, filtered through a syringe filter, and measured.

2.10. DFT calculations

All spin-polarized density functional theory (DFT + U) calculations were performed using the Vienna ab initio Simulation Package (VASP) with the projector augmented wave (PAW) method [52,53]. The Perdew-Burke-Ernzerhof (PBE) functional with the generalized gradient approximation (GGA) was used to describe the electron exchange–correlation functions [54]. A kinetic energy cutoff for the plane-wave basis set was set at 600 eV in all calculations. Brillouin zone integration was performed using Γ-point sampling with 1 × 1 × 2 k-points. The Gaussian smearing of 0.05 eV was employed [55]. The Hubbard-U term of 4.0 eV for V 3d states was chosen following previous studies [56]. The convergence criteria for electronic and atomic relaxations were set at 10^{-5} eV and 10^{-2} eV/Å, respectively. To include the effect of the van der Waals (vdW) dispersive interactions on the energetics and structural optimizations, we fully optimized the lattice parameters and atomic coordinates with the revised vdW-DF2 functional [57]. The optimized lattice parameters of V_3(PET) are $a = 19.565$ Å, $b = 19.890$ Å, $c = 11.496$ Å, $\alpha = 89.447°$, $\beta = 90.282°$, and $\gamma = 120.429°$.

In order to calculate the defect formation energy of the PET ligand, a 1 × 2 × 2 supercell was optimized using a Γ-point sampling under the same conditions. For the negatively charged ligands and frameworks, the charge neutrality was corrected by adding hydrogen atoms and hydroxide units, respectively, as a capping agent in place of each removed ligand [31]. Therefore, the ligand defect formation energy (ΔE_{defect}) is defined as

$$\Delta E_{defect} = \left(E_{defect+H_2O^*+OH^*} + E_{ligand+H^*}\right) - \left(E_{pristine} + nE_{H_2O(g)}\right) \tag{1}$$

where $E_{defect+H_2O^*+OH^*}$, $E_{ligand+H^*}$, $E_{pristine}$, $E_{H_2O(g)}$, and n are the total energies of defective V_3(PET) with capping agents, ligand with capping agents, pristine V_3(PET), gas-phase H_2O, and the number of H_2O molecules, respectively. '*' indicates the state adsorbed to the carboxylate groups. Since the ligand has six carboxylate units, twelve H_2O molecules were added for charge neutrality. For gas-phase H_2 and H_2O, we used a 30 Å × 30 Å × 30 Å supercell.

2.11. Low pressure N_2 adsorption-desorption isotherm

To analyze the Brunauer, Emmet, Teller (BET) surface area and pore diameter of activated MOFs, we measured N_2 isotherms to 1 bar at 77 K on a Tristar II Plus 3030 (Micromeritics). After the measurement of N_2 isotherms, the BET surface area was calculated using the Rouquerol criteria [58]. Pore size distribution and pore volume of activated MOFs were calculated by the DFT model with slit pore geometry using Micromeritics MicroActive control software.

2.12. High-pressure H_2 isotherm measurements

The hydrogen uptake was measured using a home-built contact cooling system integrated with a commercial Sievert-type PCT Pro-E&E (Setaram). The cooling system's cold finger is set to contact liquid nitrogen at a certain level and maintain the target temperature by transferring heat to oxygen-free copper through the heater. Adsorption and desorption isotherms were measured (0–40 bar) at various temperatures (77–298 K) in a sample cell with a volume of approximately 1.2 mL using ultra-pure hydrogen gas (99.999 %).

Before hydrogen adsorption measurements, samples were heated for 12 h at 120 °C in a vacuum to remove guest molecules in the framework. To eliminate the influence of the temperature gradient between the cooled sample cell and the gas reservoir during the isothermal measurements at cryogenic temperatures, we measured hydrogen uptake in a non-adsorbed sample (sea sand) with the same volume under the same conditions ($n_{seasand}(p,T)$). Finally, to minimize the measurement error at cryogenic temperatures and calculate the excess H_2 ($n_{exc}(p,T)$), the excess H_2 ($n_{exc}(p,T)$) can be corrected by subtracting the unadsorbed sample concentration ($n_{seasand}(p,T)$) from the measured hydrogen concentration ($n_{measured}(p,T)$), as shown in Eq. (2).

$$n_{exc}(p,T) = n_{measured}(p,T) - n_{seasand}(p,T) \tag{2}$$

Excess gravimetric uptake is the amount of hydrogen adsorption (m_{ads}) per the sum of sample mass (m_{sample}) and adsorbed hydrogen (m_{ads}).

$$\text{Excess gravimetric uptake} = \frac{m_{ads}}{m_{ads} + m_{sample}} \times 100 \tag{3}$$

Total H_2 uptake was estimated using the following equation: (total uptake) = (excess uptake) + ρV_p, where ρ is the density of H_2 at each temperature and pressure.

2.13. High-pressure H_2 adsorption/desorption cycle test

To assess the long-term stability of V_3(PET)@400 under practical operating conditions, we measured consecutive high-pressure hydrogen isotherms at 273 K over 200 cycles. The measurements were conducted using an automated controlled Sieverts apparatus (BEL-HP, BEL.JAPAN. INC) [59]. Approximately 0.5 g of the sample was activated using a Micromeritics ASAP2020 degassing instrument at 120 °C for 12 h. After activation, the sample cell was sealed with a Swagelok SS-8-VCR-2-GR-5 M stainless steel gasket. The degassed sample, within the ASAP sorption cell, was transferred to a glove box without exposure to air. Inside the glove box, the sample was loaded into the BEL-HP measurement cell. The cell was packed and tapped until no further volume change was observed. The sample cell was then sealed inside a zip-lock bag, removed from the glove box, and promptly connected to the measurement instrument to minimize exposure to moisture.

The sample was regenerated again at 120 °C for 6 h under vacuum. Subsequently, the skeletal volume of the sample at 25 °C was measured by dosing helium up to 1 bar using the BEL-HP instrument [60]. Both the skeletal volume of the sample and the dead volume of the empty cell were determined by dosing helium at 25 °C a total of 60 times, with the average values used for calculations. Following this, high-pressure hydrogen isotherm was measured up to 100 bar at 273 K using an ethylene glycol–water bath.

For the cycling tests, the sample cell was subjected to 200 cycles of pressurization to 100 bar with hydrogen and evacuation to 8×10^{-1} Pa under vacuum by sequentially opening the valves of the hydrogen gas tank and the vacuum pump. Isotherms were measured initially and after every 25 cycles. Ultra-high-purity (99.999 % purity) hydrogen and helium gases were used in all experiments. An equilibrium time of 500 s was set, and measurements proceeded to the next pressure point once the pressure change was within 0.1 % of the full-scale pressure.

3. Results and discussion

3.1. Thermal treatment and improved water stability of V_3(PET)

Bare V_3(PET) was synthesized using a solvothermal method with acetic acid as the modulator, following a previously reported procedure [47]. The crystal structure consists of a vanadium trinuclear node linked by six hexatopic peripherally extended triptycene (H_6PET) ligands. As shown in Fig. S1, the TGA plot of a V_3(PET) indicates the onset of framework decomposition around 475 °C. Motivated by this observation, we prepared a series of thermally treated samples at temperatures between 300 to 450 °C in an external tube furnace under a flowing Ar atmosphere. As shown in Fig. 1a-1c and Figs. S2-S3, samples annealed at 300 and 400 °C (referred to as V_3(PET)@300 and V_3(PET)@400) were characterized with PXRD, SEM, and Energy-dispersive X-ray spectroscopy (EDS). Both samples show no difference compared to the bare V_3(PET). Specifically, N_2 isotherm measurements (Fig. 1d-1f and Fig. S4) revealed that V_3(PET), V_3(PET)@300, and V_3(PET)@400 exhibited the same BET surface area of approximately 3,400 m^2/g, pore

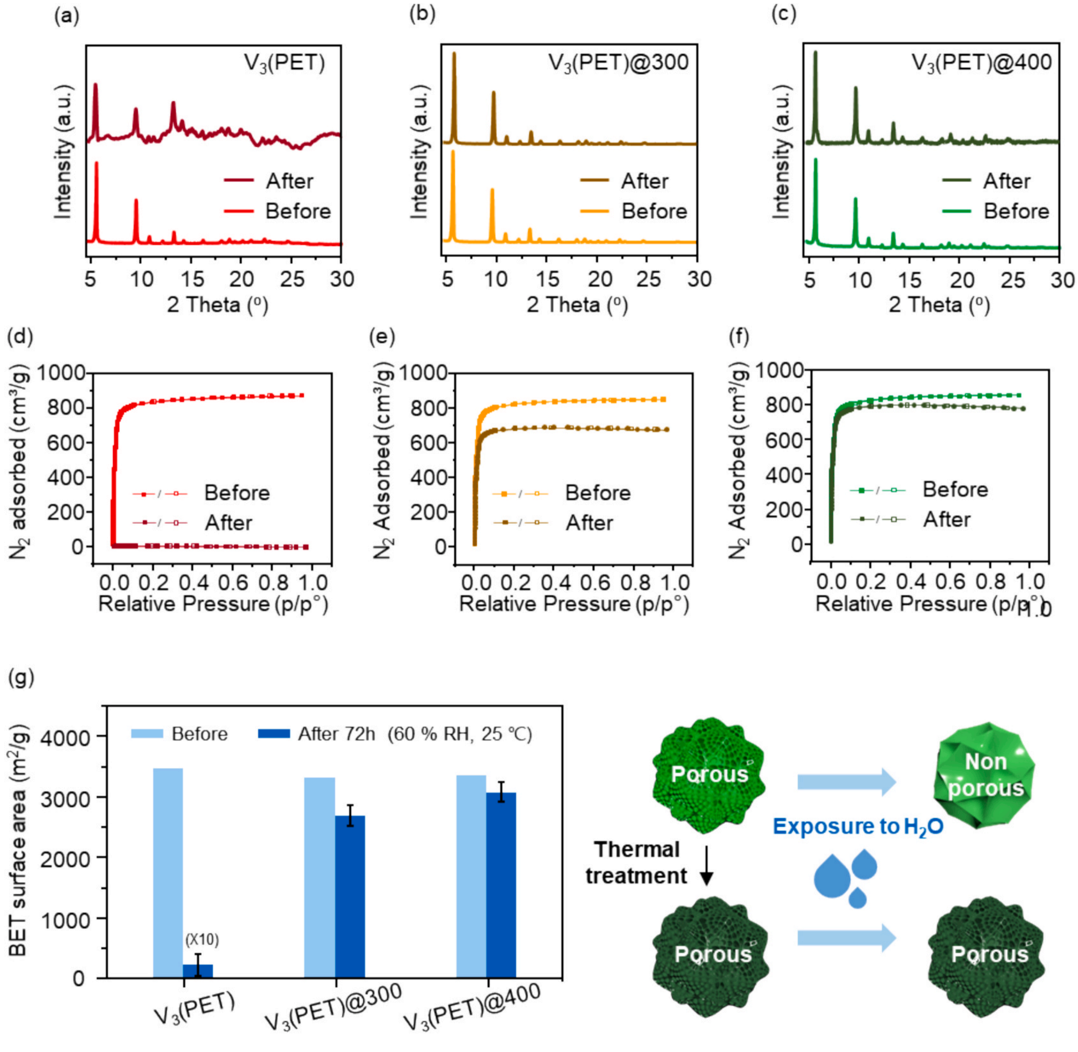

Fig. 1. PXRD patterns of (a) bare V_3(PET), (b) V_3(PET)@300, and (c) V_3(PET)@400. N_2 isotherms of (d) bare V_3(PET), (e) V_3(PET)@300, and (f) V_3(PET)@400 at 77 K (adsorption: filled symbols, desorption: empty symbols). BET surface areas of (g) V_3(PET), V_3(PET)@300 and V_3(PET)@400 before and after exposure to 60 % RH at 25 °C for 72 h.

volume of 1.36 cm^3/g and pore size of 13 Å. However, framework collapse occurred when the samples were thermally treated at a temperature over 450 °C, as shown in Fig. S5, which is in good agreement with TGA results.

In order to examine the water stability performance, bare V_3(PET), V_3(PET)@300, and V_3(PET)@400 were exposed to 60 % RH at 25 °C. For bare V_3(PET), the BET surface area became 1,247 m^2/g within 24 h and decreased by 99 % with total porosity loss after 72 h, as confirmed by the PXRD pattern (Fig. S6a and Fig. 1a) and N_2 isotherm measurement (Fig. S6b–6c and Fig. 1d). Notably, bare V_3(PET) is not stable under humid conditions, even though it is composed of hard acid metals (V^{3+})–hard base ligands (carboxylate ligands), which should confer the good water stability based on the HSAB theory. In contrast, V_3(PET)@300 and V_3(PET)@400 exhibited no significant changes in the PXRD pattern (Fig. 1b and 1c) and their BET surface area values slightly decreased by 19 % (from 3,329 m^2/g to 2,690 m^2/g) and 8 % (from 3,359 m^2/g to 3,080 m^2/g), respectively (Fig. 1e, 1f and 1 g). More interestingly, V_3(PET)@400 showed BET surface area of 3,160 m^2/g and 2,251 m^2/g, respectively, after exposure to 60 % RH for 7 days and 14 days, indicating decreases of 6 % and 33 % with no significant changes in the PXRD pattern (Fig. S7). This suggests that the thermal treatment significantly improved the water stability of V_3(PET). In particular, we

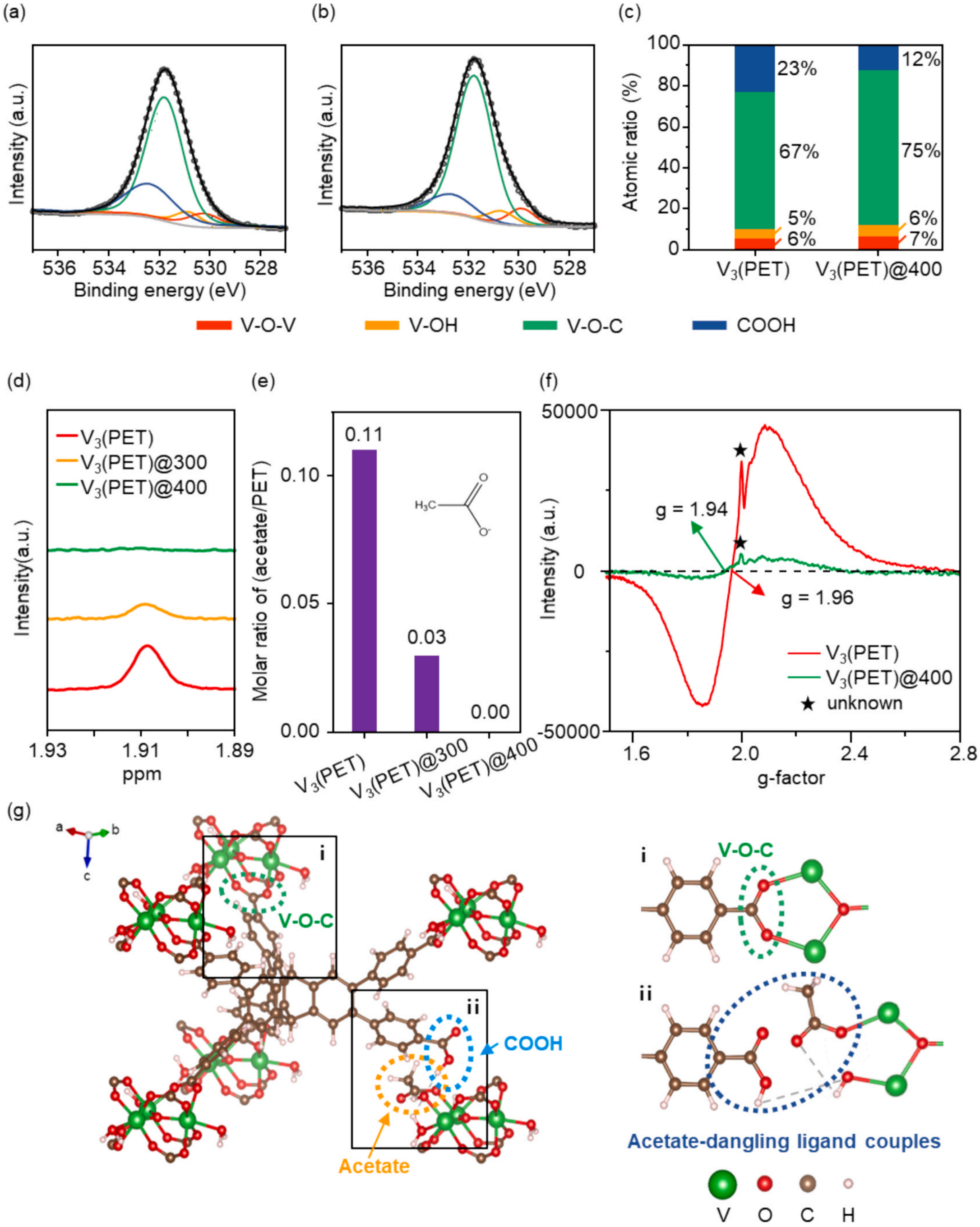

Fig. 2. High-resolution O 1 s XPS spectra of (a) bare V_3(PET) and (b) V_3(PET)@400. (c) The peak area ratio of high-resolution O 1 s XPS spectra. The peak ratios of each peak were determined through the area of the deconvoluted high-resolution O 1 s spectra. (d) Partially enlarged view of solution-state ^{1}H NMR spectra of bare V_3(PET), V_3(PET)@300, and V_3(PET)@400. (e) The molar ratio of acetate-to-PET. (f) EPR spectra of V_3(PET) and V_3(PET)@400. (g) Illustration showing V-O-C, COOH, and acetate in V_3(PET).

found that V_3(PET)@400 shows the best performance for water stability.

After determining 400 °C as a suitable thermal treatment temperature, we further investigated the effect of treatment duration on water stability (Fig. S8). The BET surface areas of the bare and thermally treated samples (1, 15, 30, and 60 min) before water exposure were similar, with values of 3,373, 3,320, 3,440, 3,359, and 3,411 m^2/g, respectively. It indicates that thermal treatment duration did not significantly alter the porosity under dry conditions. However, after exposure to 60 % RH for 3 days, the BET surface areas decreased to 41, 2,161, 2,533, 3,080, and 2,350 m^2/g, respectively. The relative decrease in BET surface area after exposure to 60 % RH for 3 days was 99, 35, 26, 8, and 31 % for the bare and thermally treated samples (1, 15, 30, and 60 min), respectively. Among these, the sample treated for 30 min exhibited the highest water stability, retaining 91.7 % of its initial surface area. This suggests that a 30 min thermal treatment is the optimal condition for improving stability under humid conditions.

3.2. *Chemical characteristics analysis of V_3(PET) and V_3(PET)@400*

Having observed the good performance of water stability in thermally treated V_3(PET) MOFs, we now address the origin of the improved water stability by thermal treatment. To do this, we conducted various analyses for bare V_3(PET) and V_3(PET)@400. Figs. S9 and S10 show NEXAFS spectroscopy and Raman analysis, respectively. Interestingly, no significant differences were observed between the two materials in terms of structural properties. Importantly, Raman analysis did not detect the G-band (~1580 cm^{-1}) or D-band (~1350 cm^{-1}), which are characteristic of carbonization products such as amorphous carbon (Fig. S10), clearly indicating the absence of carbonization. According to previous studies [25,61], the formation of carbonaceous layers can improve the water stability of MOFs by blocking water molecules; however, this mechanism is not applicable in our case due to the absence of such carbon signals. Additionally, XPS survey spectra showed no significant increase in the C/V composition ratio (Fig. S11 and Table S1), further confirming that no amorphous carbon coating was formed during thermal treatment [26].

Distinct differences were observed in the high-resolution O 1 s spectra. In Fig. 2a and 2b, the peaks at 531.6 eV and 532.9 eV correspond to V-O-C and COOH units, respectively. Thus, the peak at 531.6 eV can be attributed to the carboxylate group in ligand or acetate bound to a metal node, while the peak at 532.9 eV can be attributed to the coordinated-free carboxylate group to a metal node [62] and assigned to dangling PET ligands [63–65]. Additionally, some of the COOH units may also originate from ligands exposed on the surface [66–69]. As shown in Fig. 2c, the V-O-C (75 %) in V_3(PET)@400 is higher than that (67 %) in bare V_3(PET). Contrary to this, the COOH (12 %) atomic ratio in V_3(PET)@400 is lower than that (23 %) in bare V_3(PET). This suggests that dangling PET ligands in bare V_3(PET) become coordinated with the metal node after the thermal treatment. FT-IR analysis revealed subtle changes in the ligand's carboxyl group (Fig. S12). The peaks associated with the carboxyl group of the PET ligand at 1,257 cm^{-1} and 1,701 cm^{-1} [70–74] show a slight decrease in intensity in V_3(PET)@400 compared to V_3(PET). Based on XPS analysis, this reduction results from the dangling ligands regaining ideal bonding with the metal node after thermal treatment.

To understand the atomic-scale mechanism of the thermal treatment-induced structural recovery followed by the improved water stability, we further performed solution-state proton nuclear magnetic resonance (^{1}H NMR) analysis. In Fig. S13, we can clearly see that the ^{1}H NMR results show signals related to PET ligands [75] and solvent (DMSO-d_6, $\delta^1H = 2.50$ ppm) [76]. In addition, the signals corresponding to H_2O ($\delta^1H = 6.00$ ppm) [77,78] from the DCl solution and coordinated water in V_3(PET) were detected. The signals corresponding to residual DMF ($\delta^1H = 2.70$ ppm, 2.90 ppm) [79,80] and acetone ($\delta^1H = 2.10$ ppm) [81], which were used for the synthesis of MOFs and washing NMR tubes were also detected. Particularly, the acetate (modulator) signals for bare V_3(PET) were observed at 1.91 ppm (Fig. 2d) [82]. Based on previous studies [39,40,83,84], the modulator can remain within the MOF structure, playing a role in regulating the synthesis rate by competing with the ligand. Thus, the modulator is able to substitute the ligand site, causing a missing ligand defect (completely detached ligand from the metal node) or a dangling ligand defect (partially detached ligand, with some bonding remaining). In our system, no significant differences were observed between V_3(PET) and V_3(PET)@400 in terms of N_2 isotherm, PXRD, NEXAFS, and Raman analysis (Fig. 1, Figs. S9 and S10). This contrasts with previous MOF studies, where modulators induce missing ligand defects [41,85–89]. Therefore, due to the hexatopic nature of PET, even if acetate units bind to the ligand sites, dangling ligands—a type of ligand defect—occur rather than causing missing ligand defects. This is because when a carboxylate unit in the PET ligand is unbound from the metal node, the others remain attached, preventing the formation of the missing ligand defect. This allows the ligand to persist in the structure as a dangling ligand. A comparison of the integration values from acetate ($\delta^1H = 1.91$ ppm) and PET ($\delta^1H = 7.60$ ppm) signals shows that the acetate-to-PET ratio is 0.11 (Fig. 2e and Table S2). This means that a dangling ligand can be formed per about ten metal nodes since the number of metal nodes in the unit cell is the same as that of the PET ligand in the unit cell. According to our DFT calculations, the dangling ligands can also interact with acetate units, as shown in Fig. 2g(ii) (acetate-dangling ligand couples). Interestingly, we further found a significant reduction in the acetate signal at 1.91 ppm after thermal treatment. The acetate-to-PET ratio decreased to 0.03 in V_3(PET)@300, and notably, no acetate signal was observed in V_3(PET)@400 (Fig. 2e and Table S2). This indicates that the thermal treatment effectively reduces the number of acetate-dangling ligand couples, leading to a stable coordination environment around the metal node (Fig. 2g(i)). Our NMR simulations agree well with the experiment. The calculated ^{1}H chemical shifts related to acetate (0.34, 0.60, and 1.79 ppm) were observed in V_3(PET) with acetate-dangling ligand couples, while these were not observed in defect-free V_3(PET) (Fig. S14).

EPR spectroscopy provided supporting evidence of structural restoration. As shown in Fig. 2f, the EPR spectrum of bare V_3(PET) exhibited a signal with $g = 1.96$ and relatively high intensity, indicating the presence of acetate defect sites arising from coordination irregularities around the metal nodes [90,91]. In contrast, the g factor of V_3(PET)@400 shifted to 1.94, accompanied by a significant decrease in intensity. The decrease in g-factor and signal intensity can be observed upon defect healing in transition metal systems [92,93]. This suggests that thermal treatment effectively reduces the density of these coordination defects, reflecting the restoration of the coordination environment around the vanadium nodes.

Moreover, we performed DFT calculations to demonstrate that the dangling ligands recombine with the metal node after the removal of acetate. Our DFT calculations show that the dangling ligand rebinds to the V atoms, stabilizing the total energy by approximately 4.8 eV, as shown in Fig. S15. These results suggest that in V_3(PET) with acetate-induced dangling ligands, thermal treatment leading to acetate removal facilitates the rebinding of the dangling ligands to rebind to V atoms, thereby restoring structural stability.

Thus, combined with the results from XPS, FT-IR, NMR, EPR analyses, and DFT calculations, we expect that V_3(PET) initially forms dangling ligands induced by the acetate modulator and then the dangling ligands return to their original positions through binding to the metal nodes after thermal treatment. This thermal treatment, just like an activation thermal process, can be used to restore the useful properties of MOFs.

3.3. *The influence of acetate-dangling ligand couples on water stability*

To elucidate the effects of the acetate-dangling ligand couple on the water stability of V_3(PET), we calculated the PET ligand defect formation energies with and without the acetate-dangling ligand couple in

V_3(PET) (Fig. S16). The ligand defects are crucial for assessing the water stability of MOFs because they provide extensive active sites where water molecules can be adsorbed [31]. According to our DFT calculations, the PET ligand defect formation energy of defect-free V_3(PET) (6.34 eV) is much larger than that of V_3(PET) with the acetate-dangling ligand couple (1.96 eV). Based on Eq. (1), the positive ligand defect formation energy indicates a high resistance to the defect formation. Therefore, the calculated defect formation energy values suggest that the PET ligand defects are more likely to occur in V_3(PET) when the acetate-dangling ligand couples exist, leading to water molecules bound to the metal nodes in the presence of water. Eventually, this causes the structural collapse. This approach of correlating defect formation energy with water stability has also been demonstrated in previous studies [34,94]. These studies highlight how defect formation energies can predict structural degradation pathways in MOFs exposed to humid environments. In line with these findings, our experimental results provide consistent evidence that supports the DFT-predicted defect formation energy trends.

To experimentally validate the impact of the acetate-dangling ligand couple on water activity, we performed various analyses on V_3(PET) and V_3(PET)@400. The high-resolution O 1 s XPS analysis showed that the H_2O peak area ratio of bare V_3(PET) (16 %) is higher than that of V_3(PET)@400 (8 %) after exposure to 60 % RH at 25 °C for 72 h, indicating that more water molecules were bound within the bare V_3(PET) structure (Fig. 3a and 3b). Additionally, water vapor adsorption isotherm measurements at 298 K demonstrated that V_3(PET) exhibited a greater strong adsorption site for water compared to V_3(PET)@400 (Fig. S17). At $P/P_0 = 0.4$, the quantity of adsorbed water was 2.2 mol/mol for V_3(PET) and 1.4 mol/mol for V_3(PET)@400. According to previous studies, at a relative pressure of $P/P_0 < 0.4$, water molecules adsorb onto strong adsorption sites, which are defined as any surface species bearing a partial charge [95]. We infer that the acetate-dangling ligand couple in V_3(PET) serve as relatively strong adsorption sites, thereby increasing water uptake at $P/P_0 = 0.4$. As previously confirmed by EPR analysis, the charge imbalance and increased partial charge of the metal node, induced by coordination irregularities in the V_3(PET) due to the presence of acetate-dangling ligand couple, enhance its reactivity toward water molecules (Fig. 2f) [96]. Mass spectrometry (MS) analysis further supports these findings by revealing PET ligand detachment upon immersion in DI water (Fig. S18). V_3(PET) and V_3(PET)@400 samples were immersed in 50 mL of DI water for 24 h, followed by filtration and MS analysis of the extracted solution. The

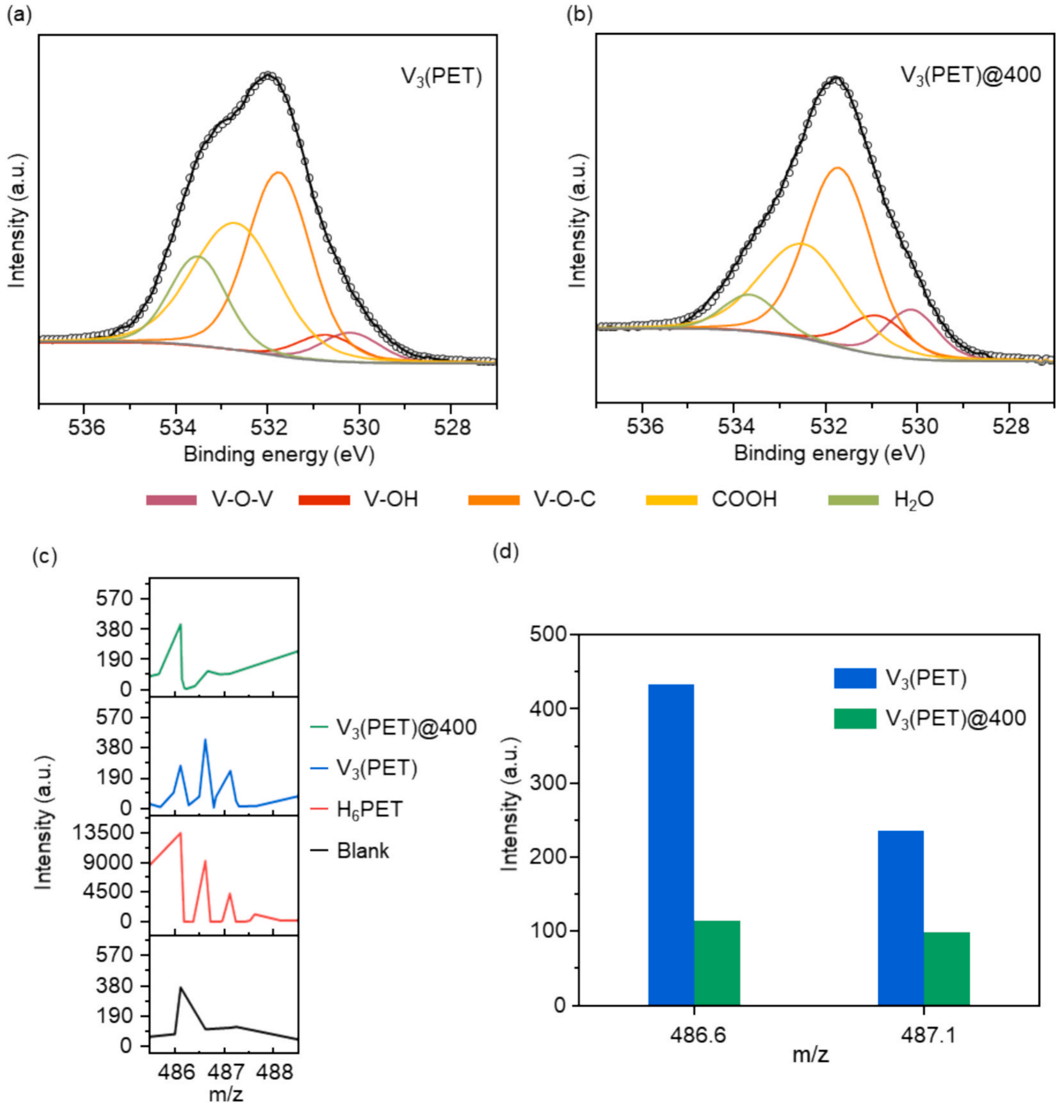

Fig. 3. High-resolution O 1 s XPS of (a) V_3(PET) and (b) V_3(PET)@400 after exposure to 60 % RH at 25 °C for 72 h, (c) Partially enlarged view of the negative ion mode mass spectra of blank, H_6PET solution and the extracted solution after V_3(PET) and V_3(PET)@400 immersion, (d) Bar graph of signal intensities obtained from the negative ion mode mass spectra of H_6PET in the extracted solution after V_3(PET) and V_3(PET)@400 immersion ($m/z = 486.6, 487.1$).

standard substance, H_6PET, was dissolved in methanol and analyzed (m/z = 486.6, 487.1) (Fig. 3c). The extracted solution from V_3(PET) immersion contained significantly more H_6PET than from V_3(PET)@400 immersion (Fig. 3d), indicating that V_3(PET) is more prone to ligand detachment in water. This aligns with our DFT calculation, which shows that V_3(PET)@400 exhibits higher ligand defect formation energy, making it more resistant to water-induced degradation.

Overall, our DFT and experimental results suggest that the acetate-dangling ligand couple creates a water-active coordination environment in V_3(PET), leading to structural instability. This finding also aligns with previous studies that emphasize the importance of strong binding energy of metal to a ligand for MOF stability under humid conditions [14].

3.4. Mechanism of thermal treatment for improving water stability

Considering our DFT calculations and experimental results, the mechanism for enhancing water stability through thermal treatment is shown in Scheme 1. Initially, the remaining modulator (acetate units) in bare V_3(PET) form the acetate-dangling ligand couples, which include coordinated-free carboxylate groups, as shown in the upper left panel of Scheme 1. When acetate units are removed by the thermal treatment, the dangling ligands can now bind to the metal nodes, creating the original hard acid metals (V^{3+})-hard base ligands (carboxylate groups) combination (the upper right panel of Scheme 1). The newly created coordination environment, resulting from the removal of modulators in the V_3(PET) framework, is resistant to water. This is the origin of the improved water stability by the thermal treatment.

To investigate the role of ligand denticity in the thermal treatment mechanism affecting water stability, we conducted comparative experiments on MOFs composed of ligands with various denticity. The thermal treatment temperature for all synthesized MOFs was determined based on TGA results, and the treatment duration was fixed at 30 min.

MIL-101, composed of a ditopic ligand (BDC), was thermally treated at 250 °C and 300 °C (Fig. S19a), resulting in the removal of acetate (Fig. S19b). However, despite this removal, the water stability of MIL-101 did not improve, as confirmed by PXRD and BET analyses before and after exposure to water (Fig. S19c and S19d). Similarly, HKUST-1, which consists of a tritopic ligand (BTC), was thermally treated at 200 and 250 °C (Fig. S20a), also resulting in acetate removal (Fig. S20b). Nevertheless, no improvement in water stability was observed (Figs. S20c and S20d). These results suggest that the proposed thermal treatment mechanism does not effectively apply to MOFs composed of low-denticity ligands. This is likely because low-denticity ligands are more prone to forming missing ligand defects rather than remaining as dangling ligands [84,98], unlike hexatopic ligands, when acetate-induced defects are generated. One point we would like to note is that the increase in the N_2 isotherm of HKUST-1 after thermal treatment suggests the formation of mesoporous defects, likely resulting from partial linker decomposition or metal node rearrangement [84,99]. However, further studies are needed to clarify this.

Cu-TCPP, which consists of a tetratopic ligand (TCPP), was thermally treated at 300 °C (Fig. S21a), leading to acetate removal (Fig. S21b). However, despite the treatment being conducted below the decomposition temperature, some of the ligand was also removed from the structure (Fig. S21b). As a result, PXRD analysis revealed a reduction in structural regularity along the a-b plane [51] (Fig. S21c), and the BET surface area decreased from 1,647 m^2/g to 517 m^2/g after thermal treatment (Fig. S21d). While the water stability showed slight improvement, the effect was less pronounced than in the hexatopic system. After water exposure, the BET surface area of Cu-TCPP decreased by 63 % (from 1,647 m^2/g to 611 m^2/g), whereas Cu-TCPP@300 exhibited only a 22 % reduction (from 517 m^2/g to 401 m^2/g) reduction (Fig. S21d). Furthermore, Raman analysis confirmed the absence of G-band or D-band signals, ruling out carbonization as a contributing factor (Fig. S21e). These findings suggest that while the proposed thermal treatment mechanism may be partially applicable to tetratopic ligand systems, additional factors influence the extent of stabilization.

Ga_3(PET), composed of hexatopic ligand (PET) and gallium, was thermally treated at 300 °C (Fig. S22a), resulting in partial removal of acetate (Fig. S22b). Water stability test results show improvement upon thermal treatment. After exposure to water, the BET surface area of Ga_3(PET) decreased by 76 % (from 3,128 m^2/g to 763 m^2/g), whereas Ga_3(PET)@300 showed only a 39 % reduction (from 2,879 m^2/g to 1,770 m^2/g) (Fig. S22c). Additionally, PXRD analysis revealed that Ga_3(PET)@300 exhibited less intensity decrease than Ga_3(PET) after water exposure, indicating better structural retention (Fig. S22d). Raman analysis confirmed the absence of carbonization effects (Fig. S22e). These results indicate that the proposed thermal treatment mechanism is most effective for MOFs composed of hexatopic ligands. Although our experimental conditions may not represent the absolute

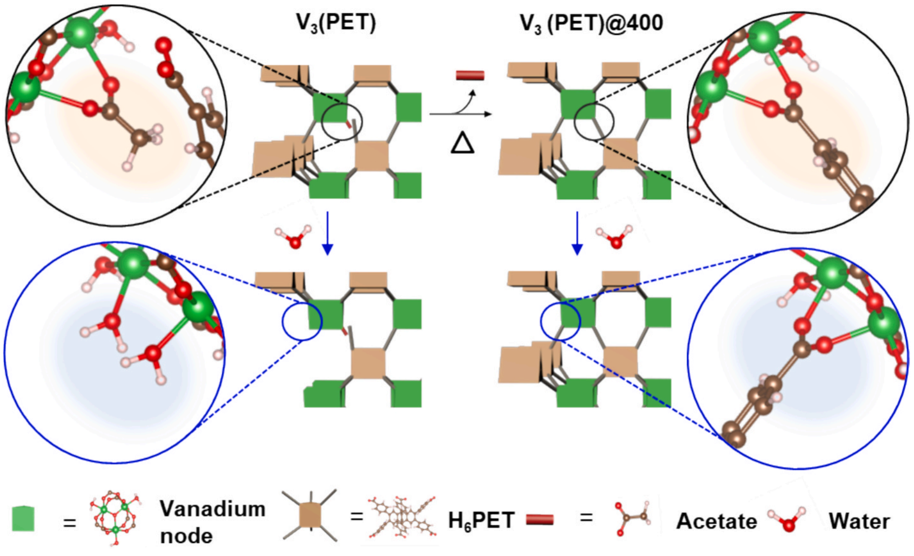

Scheme 1. Mechanism of the improved water stability by the thermal treatment in V_3(PET) with hexatopic H_6PET ligands. V_3(PET) consists of a vanadium trinuclear node linked by six hexatopic PET ligands. The connections between the metal nodes and H_6PET ligands form the acs framework [97]. The illustration before exposure to water is the activated MOF structure.

optimal parameters, the observed improvements suggest that ligand denticity plays a crucial role in determining the effectiveness of thermal treatment for enhancing water stability in MOFs. The proposed mechanism is particularly applicable to polytopic ligands with hexatopic or higher denticity, as these structures facilitate ligand reattachment and resist defect formation more effectively.

3.5. Hydrogen storage performance of V_3(PET)@400

According to our recent study [47], V_3(PET) showed good performance for hydrogen storage. Thus, we examined the hydrogen storage performance of V_3(PET)@400. We conducted the hydrogen isotherm measurement of V_3(PET)@400 at different temperatures to measure the excess hydrogen uptakes (Fig. S23) while also measuring the hydrogen adsorption isotherms of bare V_3(PET) for comparison (Fig. S24a). The total hydrogen uptakes were determined using the pore volume and bulk density of hydrogen [59,100] (Fig. 4a, Fig. S24b, and Table S3). At 77 K and 40 bars, V_3(PET)@400 showed total gravimetric and volumetric H_2 uptakes of 6.71 wt% and 36.49 g/L, respectively. As the temperature increased to 298 K, both gravimetric and volumetric uptakes of V_3(PET)@400 decreased to 0.68 wt% and 3.59 g/L, consistent with typical physisorption behavior. The hydrogen storage performance of V_3(PET)@400 retained a similar performance to bare V_3(PET), which exhibited total gravimetric and volumetric H_2 uptakes of 6.97 wt% and 37.97 g/L at 77 K and 40 bar. This indicates that the thermal treatment process did not adversely affect the hydrogen adsorption capacity of V_3(PET). In addition, these values are comparable to well-known hydrogen storage MOFs such as NU-1000 (6.41 wt%, 39.13 g/L) and HKUST-1 (4.85 wt%, 44.83 g/L) at 77 K and 40 bar, indicating that V_3(PET)@400 maintains competitive performance (Table S3).

Furthermore, to confirm the good water stability of V_3(PET)@400, the hydrogen isotherms were measured after exposure to 60 % RH at 25 °C for 3 days and 7 days, as shown in Fig. 4b and S25. After 3 days, the gravimetric and volumetric hydrogen total uptakes at 77 K and 40 bars indicate no performance loss after water exposure. Even after 7 days, the gravimetric and volumetric hydrogen total uptakes of V_3(PET)@400 indicated only 5.0 % and 5.4 % loss, respectively. Overall, V_3(PET)@400 showed excellent water stability while maintaining its original hydrogen adsorption performance.

Finally, we investigated the mechanical and long-term stability that plays a key role in the economic viability and efficiency of hydrogen storage systems [100,101]. To do this, we measured the gravimetric and volumetric total hydrogen uptakes of V_3(PET)@400 between 2 and 100 bar up to 200 adsorption–desorption cycles at 273 K, as shown in Fig. 4c. The H_2 isotherms were measured for 1st, 25th, 50th, 75th, 100th, 125th, 150th, 175th and 200th cycles (Fig. 4c and Fig. S26a). We can clearly see that the hydrogen storage performance remains consistent through all 200 cycles, indicating that the structure and the hydrogen storage performance were maintained under prolonged exposure to high pressure. This is further supported by the consistent PXRD patterns and N_2 isotherms before and after the test (Fig. S26b–S26c).

4. Conclusion

In conclusion, we propose a simple thermal treatment to improve the water stability of V_3(PET), which is composed of hexatopic ligands. We found that the poor water stability of V_3(PET) was attributed to the acetate-dangling ligand couple. By doing the thermal treatment, we successfully removed acetate units, allowing the dangling ligands to reform the strong metal–ligand bonds. This creates the original hard acid metals (V^{3+})-hard base ligands (carboxylate ligands) bond. As a result, V_3(PET)@400 exhibited only an 8 % loss in porosity after 60 % RH at

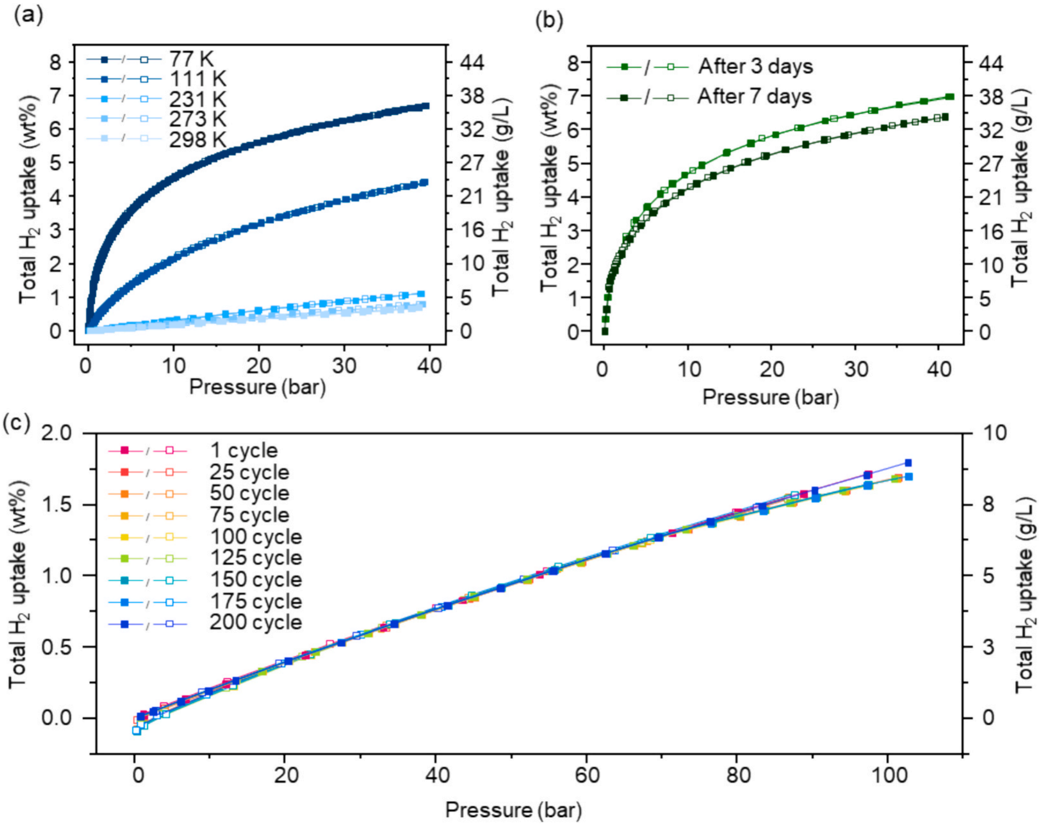

Fig. 4. (a) Gravimetric and volumetric total hydrogen uptakes of V_3(PET)@400 for different temperatures up to 40 bar. (b) Gravimetric and volumetric total hydrogen uptakes of V_3(PET)@400 after exposure to 60 % RH at 25 °C up to 40 bar. (c) Gravimetric and volumetric total hydrogen uptakes of V_3(PET)@400 for 1st, 25th, 50th, 75th, 100th, 125th, 150th, 175th, and 200th cycles from 2 bar to 100 bar at 273 K. (adsorption: filled symbols, desorption: empty symbols).

25 °C for 72 h, whereas bare V_3(PET) completely lost its crystallinity under the same conditions. Importantly, this thermal treatment enhanced water stability while preserving porosity, providing an effective approach to maintaining structural integrity in humid environments. Our DFT calculations also showed that the ligand defect formation energy in V_3(PET)@400 without the acetate-dangling ligand couples is much larger than that of bare V_3(PET), leading V_3(PET)@400 to good water stability. This stability is attributed to the ligand denticity. Notably, the thermal treatment mechanism does not effectively apply to MOFs composed of low-denticity ligands. In contrast, Cu-TCPP, which composed of tetradentate TCPP ligands, exhibited potential for enhanced water stability. Furthermore, the Ga-based hexatopic PET structure showed similar water stability phenomena to V_3(PET), suggesting that this mechanism was applicable to MOFs composed of hexatopic or higher polytopic ligands. We further found that V_3(PET)@400 maintained a comparable hydrogen storage performance to that of defect-free V_3(PET). Taken together, we believe that the understanding of the improved water stability by thermal treatment can be widely used to design new MOFs, particularly those with polytopic ligand systems, offering enhanced water stability for gas storage applications.

CRediT authorship contribution statement

Hong-Eun An: Writing – review & editing, Writing – original draft, Visualization, Validation, Methodology, Investigation, Formal analysis, Data curation. **Wan-Tae Kim:** Writing – review & editing, Writing – original draft, Visualization, Validation, Methodology, Investigation, Formal analysis, Data curation. **Dong Yun Shin:** Visualization, Validation, Investigation, Formal analysis, Data curation. **SeJin Park:** Formal analysis. **Eunki Yoon:** Formal analysis. **Dae Won Kim:** Formal analysis. **Chang Seop Hong:** Resources. **Soohyung Park:** Resources. **Hyunchul Oh:** Resources. **Jung-Hoon Lee:** Writing – review & editing, Writing – original draft, Supervision, Resources, Project administration, Funding acquisition, Conceptualization. **Sohee Jeong:** Writing – review & editing, Writing – original draft, Supervision, Resources, Project administration, Funding acquisition, Conceptualization.

Declaration of competing interest

The authors declare that they have no known competing financial interests or personal relationships that could have appeared to influence the work reported in this paper.

Acknowledgment

This research was supported by the program of Future Hydrogen Original Technology Development (2021M3I3A1083946 and 2021M3I3A1084573) through the National Research Foundation of Korea (NRF) funded by the Ministry of Science and ICT, the KU-KIST Graduate School of Converging Science and Technology (KU-KIST school program), the KIST Institutional Programs (Project No. 2E33211), and the Pioneer Research Center Program (RS-2024-00431320) through the NRF funded by the Ministry of Education, Science and Technology.

Appendix A. Supplementary data

Supplementary data to this article can be found online at https://doi.org/10.1016/j.cej.2025.163083.

Data availability

Data will be made available on request.

References

[1] M.F. Hordeski, Alternative fuels: the future of hydrogen, River Publishers, 2020.

[2] S.E. Hosseini, Hydrogen fuel, a game changer for the world's energy scenario, Int. J. Green Energy 21 (6) (2024) 1366–1382.

[3] H. Li, X. Cao, Y. Liu, Y. Shao, Z. Nan, L. Teng, W. Peng, J. Bian, Safety of hydrogen storage and transportation: An overview on mechanisms, techniques, and challenges, Energy Rep. 8 (2022) 6258–6269.

[4] J. Liu, M. Zhao, L. Rong, Overview of hydrogen-resistant alloys for high-pressure hydrogen environment: on the hydrogen energy structural materials, Clean Energy 7 (1) (2023) 99–115.

[5] A. Anastasopoulou, H. Furukawa, B.R. Barnett, H.Z. Jiang, J.R. Long, H. M. Breunig, Technoeconomic analysis of metal–organic frameworks for bulk hydrogen transportation, Energy Environ. Sci. 14 (3) (2021) 1083–1094.

[6] Z. Chen, K.O. Kirlikovali, K.B. Idrees, M.C. Wasson, O.K. Farha, Porous materials for hydrogen storage, Chem 8 (3) (2022) 693–716.

[7] H. Li, K. Wang, Y. Sun, C.T. Lollar, J. Li, H.-C. Zhou, Recent advances in gas storage and separation using metal–organic frameworks, Mater. Today 21 (2) (2018) 108–121.

[8] X. Lin, J. Jia, N. Champness, P. Hubberstey, M. Schröder, Metal-organic framework materials for hydrogen storage, Solid-State Hydrogen Storage (2008) 288–312.

[9] P. Peng, A. Anastasopoulou, K. Brooks, H. Furukawa, M.E. Bowden, J.R. Long, T. Autrey, H. Breunig, Cost and potential of metal–organic frameworks for hydrogen back-up power supply, Nat. Energy 7 (5) (2022) 448–458.

[10] A. Yuvaraj, A. Jayarama, D. Sharma, S.S. Nagarkar, S.P. Duttagupta, R. Pinto, Role of metal-organic framework in hydrogen gas storage: A critical review, Int. J. Hydrogen Energy 59 (2024) 1434–1458.

[11] T. Paul, A. Juma, R. Alqerem, G. Karanikolos, H.A. Arafat, L.F. Dumée, Scale-up of metal-organic frameworks production: engineering strategies and prospects towards sustainable manufacturing, J. Environ. Chem. Eng. (2023) 111112.

[12] G. Walker, Solid-state hydrogen storage: materials and chemistry, Elsevier, 2008.

[13] B. Liu, K. Vikrant, K.-H. Kim, V. Kumar, S.K. Kailasa, Critical role of water stability in metal–organic frameworks and advanced modification strategies for the extension of their applicability, Environ. Sci.: Nano 7 (5) (2020) 1319–1347.

[14] L. Wang, X. Li, B. Yang, K. Xiao, H. Duan, H. Zhao, The chemical stability of metal-organic frameworks in water treatments: Fundamentals, effect of water matrix and judging methods, Chem. Eng. J. 450 (2022) 138215.

[15] J. Ren, H.W. Langmi, B.C. North, M. Mathe, Review on processing of metal–organic framework (MOF) materials towards system integration for hydrogen storage, Int. J. Energy Res. 39 (5) (2015) 607–620.

[16] Y. An, X. Lv, W. Jiang, L. Wang, Y. Shi, X. Hang, H. Pang, The stability of MOFs in aqueous solutions—Research progress and prospects, Green Chem, Eng, 2023.

[17] X. Qian, R. Zhang, L. Chen, Y. Lei, A. Xu, Surface hydrophobic treatment of water-sensitive DUT-4 metal–organic framework to enhance water stability for hydrogen storage, ACS Sustainable Chem. Eng. 7 (19) (2019) 16007–16012.

[18] M. Kang, J.E. Kim, D.W. Kang, H.Y. Lee, D. Moon, C.S. Hong, A diamine-grafted metal–organic framework with outstanding CO_2 capture properties and a facile coating approach for imparting exceptional moisture stability, J. Mater. Chem. A 7 (14) (2019) 8177–8183.

[19] W. Zhang, Y. Hu, J. Ge, H.-L. Jiang, S.-H. Yu, A facile and general coating approach to moisture/water-resistant metal–organic frameworks with intact porosity, J. Am. Chem. Soc. 136 (49) (2014) 16978–16981.

[20] S. Yang, L. Peng, D.T. Sun, M. Asgari, E. Oveisi, O. Trukhina, S. Bulut, A. Jamali, W.L. Queen, A new post-synthetic polymerization strategy makes metal–organic frameworks more stable, Chem. Sci. 10 (17) (2019) 4542–4549.

[21] F. Drache, V. Bon, I. Senkovska, C. Marschelke, A. Synytska, S. Kaskel, Postsynthetic inner-surface functionalization of the highly stable zirconium-based metal–organic framework DUT-67, Inorg. Chem. 55 (15) (2016) 7206–7213.

[22] J.G. Nguyen, S.M. Cohen, Moisture-resistant and superhydrophobic metal−organic frameworks obtained via postsynthetic modification, J. Am. Chem. Soc. 132 (13) (2010) 4560–4561.

[23] T. Wittmann, R. Siegel, N. Reimer, W. Milius, N. Stock, J. Senker, Enhancing the water stability of Al-MIL-101-NH_2 via postsynthetic modification, Chem. Eur. J. 21 (1) (2015) 314–323.

[24] E. Falcone, P. Faller, Thermodynamics-based rules of thumb to evaluate the interaction of chelators and kinetically-labile metal ions in blood serum and plasma, Dalton Trans. 52 (8) (2023) 2197–2208.

[25] S.J. Yang, C.R. Park, Preparation of highly moisture-resistant black-colored metal organic frameworks, Adv. Mater. 24 (29) (2012) 4010–4013.

[26] S. Tanaka, Y. Tanaka, A simple step toward enhancing hydrothermal stability of ZIF-8, ACS Omega 4 (22) (2019) 19905–19912.

[27] M. Ding, X. Cai, H.-L. Jiang, Improving MOF stability: approaches and applications, Chem. Sci. 10 (44) (2019) 10209–10230.

[28] J.J. Low, A.I. Benin, P. Jakubczak, J.F. Abrahamian, S.A. Faheem, R.R. Willis, Virtual high throughput screening confirmed experimentally: porous coordination polymer hydration, J. Am. Chem. Soc. 131 (43) (2009) 15834–15842.

[29] X. Zhang, B. Wang, A. Alsalme, S. Xiang, Z. Zhang, B. Chen, Design and applications of water-stable metal-organic frameworks: status and challenges, Coord. Chem. Rev. 423 (2020) 213507.

[30] C. Chen, Z. Yu, D.S. Sholl, K.S. Walton, Effect of Loading on the Water Stability of the Metal–Organic Framework DMOF-1 [Zn(bdc)(dabco)$_{0.5}$], J. Phys. Chem. Lett. 13 (22) (2022) 4891–4896.

[31] S. Jamdade, Z. Yu, S.E. Boulfelfel, X. Cai, R. Thyagarajan, H. Fang, D.S. Sholl, Probing Structural Defects in MOFs Using Water Stability, J. Phys. Chem. C (2024).

[32] D.S. Sholl, R.P. Lively, Defects in metal–organic frameworks: challenge or opportunity? J. Phys. Chem. Lett. 6 (17) (2015) 3437–3444.

[33] X. Wang, L. Zhai, Y. Wang, R. Li, X. Gu, Y.D. Yuan, Y. Qian, Z. Hu, D. Zhao, Improving water-treatment performance of zirconium metal-organic framework membranes by postsynthetic defect healing, ACS Appl. Mater. Interfaces 9 (43) (2017) 37848–37855.

[34] C. Zhang, C. Han, D.S. Sholl, J. Schmidt, Computational characterization of defects in metal–organic frameworks: Spontaneous and water-induced point defects in ZIF-8, J. Phys. Chem. Lett. 7 (3) (2016) 459–464.

[35] F.E. Chen, T.A. Pitt, D.J. Okong'o, L.G. Wetherbee, J.J. Fuentes-Rivera, P. J. Milner, A structure–activity study of aromatic acid modulators for the synthesis of zirconium-based metal–organic frameworks, Chem. Mater. 34 (7) (2022) 3383–3394.

[36] S. Dissegna, K. Epp, W.R. Heinz, G. Kieslich, R.A. Fischer, Defective metal-organic frameworks, Adv. Mater. 30 (37) (2018) 1704501.

[37] D. Jiang, C. Huang, J. Zhu, P. Wang, Z. Liu, D. Fang, Classification and role of modulators on crystal engineering of metal organic frameworks (MOFs), Coord. Chem. Rev. 444 (2021) 214064.

[38] K. Tan, H. Pandey, H. Wang, E. Velasco, K.-Y. Wang, H.-C. Zhou, J. Li, T. Thonhauser, Defect termination in the UiO-66 family of metal–organic frameworks: the role of water and modulator, J. Am. Chem. Soc. 143 (17) (2021) 6328–6332.

[39] Y. Huang, Y. Jiao, T. Chen, Y. Gong, S. Wang, Y. Liu, D.S. Sholl, K.S. Walton, Tuning the wettability of metal–organic frameworks via defect engineering for efficient oil/water separation, ACS Appl. Mater. Interfaces 12 (30) (2020) 34413–34422.

[40] Y. Kondo, Y. Kuwahara, K. Mori, H. Yamashita, Dual role of missing-linker defects terminated by acetate ligands in a zirconium-based MOF in promoting photocatalytic hydrogen peroxide production, J. Phys. Chem. C 125 (51) (2021) 27909–27918.

[41] F. Vermoortele, B. Bueken, G. Le Bars, B. Van de Voorde, M. Vandichel, K. Houthoofd, A. Vimont, M. Daturi, M. Waroquier, V. Van Speybroeck, Synthesis modulation as a tool to increase the catalytic activity of metal–organic frameworks: the unique case of UiO-66 (Zr), J. Am. Chem. Soc. 135 (31) (2013) 11465–11468.

[42] G. Cai, H.L. Jiang, A modulator-induced defect-formation strategy to hierarchically porous metal–organic frameworks with high stability, Angew. Chem. 56 (2) (2017) 563–567.

[43] J. Wang, L. Liu, C. Chen, X. Dong, Q. Wang, L. Alfilfil, M.R. AlAlouni, K. Yao, J. Huang, D. Zhang, Engineering effective structural defects of metal–organic frameworks to enhance their catalytic performances, J. Mater. Chem. A 8 (8) (2020) 4464–4472.

[44] J. Choi, L.-C. Lin, J.C. Grossman, Role of structural defects in the water adsorption properties of MOF-801, J. Phys. Chem. C 122 (10) (2018) 5545–5552.

[45] J.A. Greathouse, M.D. Allendorf, The interaction of water with MOF-5 simulated by molecular dynamics, J. Am. Chem. Soc. 128 (33) (2006) 10678–10679.

[46] K. Tan, N. Nijem, Y. Gao, S. Zuluaga, J. Li, T. Thonhauser, Y.J. Chabal, Water interactions in metal organic frameworks, Cryst. Eng. Comm. 17 (2) (2015) 247–260.

[47] W.-T. Kim, W.-G. Lee, H.-E. An, H. Furukawa, W. Jeong, S.-C. Kim, J.R. Long, S. Jeong, J.-H. Lee, Machine learning-assisted design of metal–organic frameworks for hydrogen storage: A high-throughput screening and experimental approach, Chem. Eng. J. 160766 (2025).

[48] S. Biswas, S. Couck, M. Grzywa, J.F. Denayer, D. Volkmer, P. Van Der Voort, Vanadium Analogues of Nonfunctionalized and Amino-Functionalized MOFs with MIL-101 Topology–Synthesis, Characterization, and Gas Sorption Properties, Eur. J. Inorg. Chem. 2012 (15) (2012) 2481–2486.

[49] R. Ediati, M.A. Setyani, D.O. Sulistiono, E. Santoso, D. Hartanto, M.M.A. B. Abdullah, Optimization of the use of mother liquor in the synthesis of HKUST-1 and their performance for removal of chromium (VI) in aqueous solutions, J. Water Process Eng. 39 (2021) 101670.

[50] C.J. Wijaya, S. Ismadji, H.W. Aparamarta, S. Gunawan, Statistically optimum HKUST-1 synthesized by room temperature coordination modulation method for the adsorption of crystal violet dye, Molecules 26 (21) (2021) 6430.

[51] X. Xu, C.-H. Li, H. Zhang, X.-M. Guo, Construction of electrochemical and photoelectrochemical sensing platform based on porphyrinic metal-organic frameworks for determination of ascorbic acid, Nanomaterials 12 (3) (2022) 482.

[52] G. Kresse, D. Joubert, From ultrasoft pseudopotentials to the projector augmented-wave method, Phys. Rev. B 59 (3) (1999) 1758–1775.

[53] P.E. Blöchl, Projector augmented-wave method, Phys. Rev. B 50 (24) (1994) 17953–17979.

[54] J.P. Perdew, K. Burke, M. Ernzerhof, Generalized gradient approximation made simple, Phys. Rev. Lett. 77 (18) (1996) 3865–3868.

[55] C. Elsässer, M. Fähnle, C.T. Chan, K. Ho, Density-functional energies and forces with Gaussian-broadened fractional occupations, Phys. Rev. B 49 (19) (1994) 13975–13978.

[56] M. Stanke, E. Palikot, L. Adamowicz, Algorithms for calculating mass-velocity and Darwin relativistic corrections with n-electron explicitly correlated Gaussians with shifted centers, J. Chem. Phys. 144 (17) (2016).

[57] I. Hamada, van der Waals density functional made accurate, Phys. Rev. B 89 (12) (2014) 121103.

[58] J.W. Osterrieth, J. Rampersad, D. Madden, N. Rampal, L. Skoric, B. Connolly, M. D. Allendorf, V. Stavila, J.L. Snider, R. Ameloot, How reproducible are surface areas calculated from the BET equation? Adv. Mater. 34 (27) (2022) 2201502.

[59] D.W. Kim, Y. Chen, H. Kim, N. Kim, Y.H. Lee, H. Oh, Y.G. Chung, C.S. Hong, High Hydrogen Storage in Trigonal Prismatic Monomer-Based Highly Porous Aromatic Frameworks, Adv. Mater. 2401739 (2024).

[60] G.E. Decker, E.D. Bloch, Using helium pycnometry to study the apparent densities of metal–organic frameworks, ACS Appl. Mater. Interfaces 13 (44) (2021) 51925–51932.

[61] A. Dychalska, P. Popielarski, W. Franków, K. Fabisiak, K. Paprocki, M. Szybowicz, Study of CVD diamond layers with amorphous carbon admixture by Raman scattering spectroscopy, Mater. Sci.-Pol. 33 (4) (2015) 799–805.

[62] Y. Wang, L. Li, P. Dai, L. Yan, L. Cao, X. Gu, X. Zhao, Missing-node directed synthesis of hierarchical pores on a zirconium metal–organic framework with tunable porosity and enhanced surface acidity via a microdroplet flow reaction, J. Mater. Chem. A 5 (42) (2017) 22372–22379.

[63] A.K. Cheetham, T.D. Bennett, F.-X. Coudert, A.L. Goodwin, Defects and disorder in metal organic frameworks, Dalton Trans. 45 (10) (2016) 4113–4126.

[64] E. Massahud, H. Ahmed, R. Babarao, Y. Ehrnst, H. Alijani, C. Darmanin, B. J. Murdoch, A.R. Rezk, L.Y. Yeo, Acoustomicrofluidic Defect Engineering and Ligand Exchange in ZIF-8 Metal–Organic Frameworks, Small Methods 7 (6) (2023) 2201170.

[65] T.-H. Park, A.J. Hickman, K. Koh, S. Martin, A.G. Wong-Foy, M.S. Sanford, A. J. Matzger, Highly dispersed palladium (II) in a defective metal–organic framework: application to C–H activation and functionalization, J. Am. Chem. Soc. 133 (50) (2011) 20138–20141.

[66] D.N.G. Krishna, J. Philip, Review on surface-characterization applications of X-ray photoelectron spectroscopy (XPS): Recent developments and challenges, Appl. Surf. Sci. Adv. 12 (2022) 100332.

[67] A.S. Racz, M. Menyhard, XPS depth profiling of nano-layers by a novel trial-and-error evaluation procedure, Sci. Rep. 14 (1) (2024) 18497.

[68] S. Wang, C.M. McGuirk, A. d'Aquino, J.A. Mason, C.A. Mirkin, Metal–organic framework nanoparticles, Adv. Mater. 30 (37) (2018) 1800202.

[69] C.V. McGuire, R.S. Forgan, The surface chemistry of metal–organic frameworks, Chem. Commun. 51 (25) (2015) 5199–5217.

[70] M.R. Shaik, S.F. Adil, Z.A. ALOthman, O.M. Alduhaish, Fumarate based metal–organic framework: an effective catalyst for the transesterification of used vegetable oil, Crystals 12 (2) (2022) 151.

[71] S. Javanbakht, M. Pooresmaeil, H. Hashemi, H. Namazi, Carboxymethylcellulose capsulated Cu-based metal-organic framework-drug nanohybrid as a pH-sensitive nanocomposite for ibuprofen oral delivery, Int. J. Biol. Macromol. 119 (2018) 588–596.

[72] D. Garg, H. Rekhi, H. Kaur, K. Singh, A.K. Malik, A novel method for the synthesis of MOF-199 for sensing and photocatalytic applications, J. Fluoresc. 32 (3) (2022) 1171–1188.

[73] M. Radhika, B. Gopalakrishna, K. Chaitra, L.K.G. Bhatta, K. Venkatesh, M. S. Kamath, N. Kathyayini, Electrochemical studies on Ni, Co & Ni/Co-MOFs for high-performance hybrid supercapacitors, Mater. Res. Express 7 (5) (2020) 054003.

[74] R.H. Alzard, L.A. Siddig, N.I. Saleh, H.L. Nguyen, Q.A.T. Nguyen, T.H. Ho, V. Q. Bui, K. Sethupathi, P. Sreejith, A. Alzamly, A new mode of luminescence in lanthanide oxalates metal–organic frameworks, Sci. Rep. 12 (1) (2022) 18812.

[75] P. Li, P. Li, M.R. Ryder, Z. Liu, C.L. Stern, O.K. Farha, J.F. Stoddart, Interpenetration isomerism in triptycene-based hydrogen-bonded organic frameworks, Angew. Chem. 131 (6) (2019) 1678–1683.

[76] S. Hu, F. Horii, H. Odani, ^{1}H NMR Study of the Solvation and Gelation in a Poly (vinyl alcohol)/DMSO-d_6/H_2 0 System, Bull. Inst. Chem. Res., Kyoto Univ. 67 (5–6) (1990) 239–248.

[77] L. Liu, H. Mo, S. Wei, D. Raftery, Quantitative analysis of urea in human urine and serum by 1 H nuclear magnetic resonance, Analyst 137 (3) (2012) 595–600.

[78] Y. Moon, R.Y. Hwang, S. Park, O.H. Han, ^{1}H NMR spectroscopy of degraded perfluorosulfonic acid membranes: A simple methodology for detecting onset of degradation, J. Electroanal. Chem. 932 (2023) 117268.

[79] M. Alves, Carbon dioxide and vegetable oil for the synthesis of bio-based polymer precursors, Université de Bordeaux, Université de Liège, 2016.

[80] A.C. Matsheku, R. Tia, M.C. Maumela, B.C. Makhubela, Ferrocenylimine Palladium (II) Complexes: Synthesis, Characterization and Application in Mizoroki-Heck and Suzuki-Miyaura Cross-Coupling Reactions, Catalysts 11 (7) (2021) 755.

[81] S.P. Kelley, P.S. Barber, P.H. Mullins, R.D. Rogers, Structural clues to UO_2^{2+}/VO_2^+ competition in seawater extraction using amidoxime-based extractants, Chem. Commun. 50 (83) (2014) 12504–12507.

[82] J. Duncan, D. Sengupta, S. Bose, K.O. Kirlikovali, O.K. Farha, Defect-induced confinement in zirconium metal-organic frameworks for enhanced hydrogen adsorption, Sus. Chem. Environ. 3 (2023) 100032.

[83] A.K. Kar, R. Sarkar, A.K. Manal, R. Kumar, S. Chakraborty, R. Ahuja, R. Srivastava, Unveiling and understanding the remarkable enhancement in the catalytic activity by the defect creation in UIO-66 during the catalytic transfer hydrodeoxygenation of vanillin with isopropanol, Appl. Catal., B 325 (2023) 122385.

[84] S.-Y. Kim, A.-R. Kim, J.W. Yoon, H.-J. Kim, Y.-S. Bae, Creation of mesoporous defects in a microporous metal-organic framework by an acetic acid-fragmented linker co-assembly and its remarkable effects on methane uptake, Chem. Eng. J. 335 (2018) 94–100.

[85] G.C. Shearer, S. Chavan, S. Bordiga, S. Svelle, U. Olsbye, K.P. Lillerud, Defect engineering: tuning the porosity and composition of the metal–organic

framework UiO-66 via modulated synthesis, Chem. Mater. 28 (11) (2016) 3749–3761.

[86] O.V. Gutov, M.G. Hevia, E.C. Escudero-Adan, A. Shafir, Metal–organic framework (MOF) defects under control: insights into the missing linker sites and their implication in the reactivity of zirconium-based frameworks, Inorg. Chem. 54 (17) (2015) 8396–8400.

[87] M. Vandichel, J. Hajek, F. Vermoortele, M. Waroquier, D.E. De Vos, V. Van Speybroeck, Active site engineering in UiO-66 type metal–organic frameworks by intentional creation of defects: a theoretical rationalization, CrstEngComm 17 (2) (2015) 395–406.

[88] S.-Q. Wang, X. Wang, X.-M. Cheng, J. Ma, W.-Y. Sun, Tailoring defect-type and ligand-vacancies in Zr (iv) frameworks for CO_2 photoreduction, J. Mater. Chem. A 10 (31) (2022) 16396–16402.

[89] J. Yin, Z. Kang, Y. Fu, W. Cao, Y. Wang, H. Guan, Y. Yin, B. Chen, X. Yi, W. Chen, Molecular identification and quantification of defect sites in metal-organic frameworks with NMR probe molecules, Nat. Commun. 13 (1) (2022) 5112.

[90] D.G. Lee, J.W. Baek, J.H. Lee, H.J. Lee, Y.H. Seo, J. Lee, C.G. Lee, B.Y. Lee, Replacement of the common chromium source $CrCl_3(thf)_3$ with well-defined $[CrCl_2(\mu\text{-}Cl)(thf)_2]_2$, Molecules 26 (4) (2021) 1167.

[91] K. Das, S. Goswami, B.B. Beyene, A.W. Yibeltal, E. Garribba, A. Frontera, A. Datta, EPR, DFT and electrochemical interpretation of a Cu (II) derivative incorporating a Schiff base precursor, Polyhedron 159 (2019) 323–329.

[92] S. Wang, L. Pan, J.-J. Song, W. Mi, J.-J. Zou, L. Wang, X. Zhang, Titanium-defected undoped anatase TiO_2 with p-type conductivity, room-temperature ferromagnetism, and remarkable photocatalytic performance, JACS 137 (8) (2015) 2975–2983.

[93] G. Ahmed, F. Raziq, M. Hanif, J. Khan, K.S. Munawar, M. Wu, X. Cao, Z. Liu, Oxygen-cluster-modified anatase with graphene leads to efficient and recyclable photo-catalytic conversion of CO_2 to CH_4 supported by the positron annihilation study, Sci. Rep. 9 (1) (2019) 13103.

[94] S. Jamdade, Z. Yu, S.E. Boulfelfel, X. Cai, R. Thyagarajan, H. Fang, D.S. Sholl, Probing structural defects in MOFs using water stability, J. Phys. Chem. C 128 (9) (2024) 3975–3984.

[95] M. Yuan, M. Gao, Q. Shi, J. Dong, Understanding the characteristics of water adsorption in zeolitic imidazolate framework-derived porous carbon materials, Chem. Eng. J. 379 (2020) 122412.

[96] S.C. Moore, M.R. Smith, J.L. Trettin, R.A. Yang, M.L. Sarazen, Kinetic impacts of defect sites in metal–organic framework catalysts under varied driving forces, ACS Energy Lett. 8 (3) (2023) 1397–1407.

[97] H. Jiang, D. Alezi, M. Eddaoudi, A reticular chemistry guide for the design of periodic solids, Nat. Rev. Mater. 6 (6) (2021) 466–487.

[98] Y. Zhang, C. Sun, Y. Ji, K. Bi, H. Tian, B. Wang, Engineering linker-defects of MIL-101 series metal organic frameworks for boosted Yb (III) adsorption, Sep. Purif. Technol. 330 (2024) 125293.

[99] F. Rouhani, P. Mousavifard, Tenfold increase in adsorption capacity of HKUST-1 toward Congo red by producing defective MOF under controlled thermal treatment, Sep. Purif. Technol. 320 (2023) 124230.

[100] D.W. Kim, M. Jung, D.Y. Shin, N. Kim, J. Park, J.-H. Lee, H. Oh, C.S. Hong, Fine-tuned MOF-74 type variants with open metal sites for high volumetric hydrogen storage at near-ambient temperature, Chem. Eng. J. 489 (2024) 151500.

[101] T.C. Wang, J.L. White, B. Bie, H. Deng, J. Edgington, J.D. Sugar, V. Stavila, M. D. Allendorf, Design Rules for Metal-Organic Framework Stability in High-Pressure Hydrogen Environments, ChemPhysChem 20 (10) (2019) 1305–1310.